Opto-Electronic Advances

Article

May 2025, Vol. 8, No. 5

DOI: 10.29026/oea.2025.240250 CSTR: 32247.14.oea.2025.240250

Terahertz active multi-channel vortices with parity symmetry breaking and near/far field multiplexing based on a dielectric-liquid crystal-plasmonic metadevice

Yiming Wang[1], Fei Fan[1,2]*, Huijun Zhao[1], Yunyun Ji[2], Jing Liu[1] and Shengjiang Chang[2]

Vortex beams carrying orbital angular momentum (OAM) are of great significance for high-capacity communication and super-resolution imaging. However, there is a huge gap between the free-space vortices (FVs) and plasmonic vortices (PVs) on chips, and active manipulation as well as multiplexing in more channels have become a pressing demand. In this work, we demonstrate a terahertz (THz) cascaded metadevice composed of a helical plasmonic metasurface, a liquid crystal (LC) layer, and a helical dielectric metasurface. By spin-orbital angular momentum coupling and photon state superposition, PVs and FVs are generated with mode purity of over 85% on average. Due to the inversion asymmetric design of the helical metasurfaces, the parity symmetry breaking of OAM is realized (the topological charge numbers no longer occur in positive and negative pairs, but all are positive), generating 6 independent channels associated with the decoupled spin states and the near-/far- field positions. Moreover, by the LC integration, dynamic mode switching and energy distribution can be realized, finally obtaining up to 12 modes with a modulation ratio of above 70%. This active tuning and multi-channel multiplexing metadevice establishes a bridge connection between the PVs and FVs, exhibiting promising applications in THz communication, intelligent perception, and information processing.

Keywords: terahertz; optical vortex; plasmonic metasurface; near/far field; multi-channel; liquid crystal

Wang YM, Fan F, Zhao HJ et al. Terahertz active multi-channel vortices with parity symmetry breaking and near/far field multiplexing based on a dielectric-liquid crystal-plasmonic metadevice. *Opto-Electron Adv* **8**, 240250 (2025).

Introduction

Terahertz (THz, 1 THz= 10^{12} Hz) waves have significant prospects in the field of next-generation communications, high-resolution imaging, and substance detection[1,2]. The spin angular momentum (SAM) and orbital angular momentum (OAM) of photons have been extended to the dimensions of optical communication and information processing due to their inherent orthogonality. Increasing attention has been brought to the vortices carrying above two angular momentums, with a donut-shaped intensity distribution and helical phase distribution, promising a wide range of applications from rotating particles to high-capacity data transmission[3,4]. In recent years, various vortex devices have been extensively studied, including free space vortices (FVs)

[1]Institute of Modern Optics, Nankai University, Tianjin Key Laboratory of Micro-scale Optical Information Science and Technology, Tianjin 300350, China; [2]Tianjin Key Laboratory of Optoelectronic Sensor and Sensing Network Technology, Tianjin 300350, China.

*Correspondence: F Fan, E-mail: fanfei@nankai.edu.cn

Received: 2 March 2024; Accepted: 22 July 2024; Published online: 6 March 2025

Open Access This article is licensed under a Creative Commons Attribution 4.0 International License.
To view a copy of this license, visit http://creativecommons.org/licenses/by/4.0/.

© The Author(s) 2025. Published by Institute of Optics and Electronics, Chinese Academy of Sciences.

and plasmonic vortices (PVs). Similarly to FVs in far-field (FF) channels[5,6], PVs exhibit strongly confined OAM characteristics in near-field (NF) channels with subwavelength dimensions[7,8], which contributes to the integration of optical systems. Unfortunately, most THz vortex devices are currently trapped in only a single vortex type with limited degrees of freedom, fixed functions, and insufficient tunability. To achieve arbitrary manipulation of vortices, it is a continuing trend in developing general strategies for multi-parameter manipulation, more independent channels, and active regulation of the operating states.

Metasurfaces composed of subwavelength microstructures show an outstanding wavefront engineering capability. Benefitting from arrays of meta-atoms with meticulous design and arrangement, wave-manipulation functionalities are realized for free space waves[9–11] and surface plasmonic waves (SPWs)[12–14]. Especially, the geometric phase metasurface provides the fundamental link between SAM and OAM, enabling excitations of FVs[15,16] and PVs[17,18] through spin-orbital angular momentum coupling. However, the OAM output state mapped by the SAM is parity symmetric and constrained to odd and even values (the topological charge numbers are additive inverse corresponding to different spin states). In addition, by responding to input spin photons, plasmonic metasurfaces based on the dynamic phase only produce PVs with restricted OAM differences[19,20]. It is worth noting that these non-independent vortex modes inevitably result in limitations for multiplexing. To solve this issue, merging both the geometric and dynamic phases with structural asymmetry can obtain spin-independent FVs[21–23] and PVs[24–26]. For example, Yuan et al investigated slit-based plasmonic metasurfaces to generate spin-decouple PVs[25]. Progress in multi-channel vortex generation and OAM multiplexing in the FF channels has been reported[27–29]. For example, an all-dielectric metasurface with polarization-selective vortex modes has been investigated by Liu et al[30]. Establishing a bridge connection between NF and FF provides more channels, and recent studies in the visible and near-infrared bands demonstrate the realizability of NF/FF multiplexing, which yields unprecedented freedom in optical field manipulation[31,32]. Despite these advances, existing vortex devices are limited to a single spin state[31], or the NF and FF vortex generation are separately associated with the different spin states[32], and in the THz band, these advances have not even been involved. Therefore, the exploration of a more refined NF/FF multiplexing mechanism is still required, especially in the THz band.

Furthermore, active manipulation of vortex beams is highly required[33]. The introduction of functional materials into microstructures provides a dynamic control strategy for THz waves[34,35], but most of them lack experimental support. Thanks to significant tunable uniaxial anisotropy, the integration of liquid crystals (LC) has been widely used for active manipulation of free space wavefronts, including beam deflectors[36,37], holograms[38,39], and lenses[40,41]. A tunable THz polarization vortex beam generator based on an LC metasurface was proposed by Wang et al, capable of generating cylindrical vector beams[42]. Zhao et al demonstrated a chiral LC cascaded metasurface, serving as a THz broadband vector vortex beam converter[43]. However, to our knowledge, there are few reports on the active manipulation of PVs. Fortunately, it has been demonstrated that LC is effective for the modulation of surface plasmonic wavefront. Wang et al took the lead in demonstrating the LC-integrated on-chip metadevice for broadband focusing and the active modulation of surface waves[44]. Therefore, the LC configuration presents great potential in facilitating the active modulation of THz NF and FF distributions.

In this work, an active multi-channel vortex generator based on a dielectric-liquid crystal-plasmonic metadevice with spin decoupling and NF/FF multiplexing has been demonstrated in the THz regime, which mainly consists of three cascaded parts as shown in Fig. 1(a): a helical dielectric metasurface, an LC layer, and a helical plasmonic metasurface. The helical plasmonic metasurface generates both PVs and FVs with multiple independent NF and FF channels with different responses of photonic spin incidences. To further break the parity conservation of FV modes, cascading a spin-decoupled dielectric metasurface in the front of the plasmonic metasurface offers an approach to leading the FV and PV states with different topological charge numbers. Moreover, the integrated LC configuration introduces an approach for spin conversion, contributing to obtaining 12 independent vortex modes and the active energy distributions among them.

Results and discussion

Single plasmonic metasurface

The structure of the proposed metadevice, is shown in Fig. 1(b), which consists of parts listed as follows: 1) The

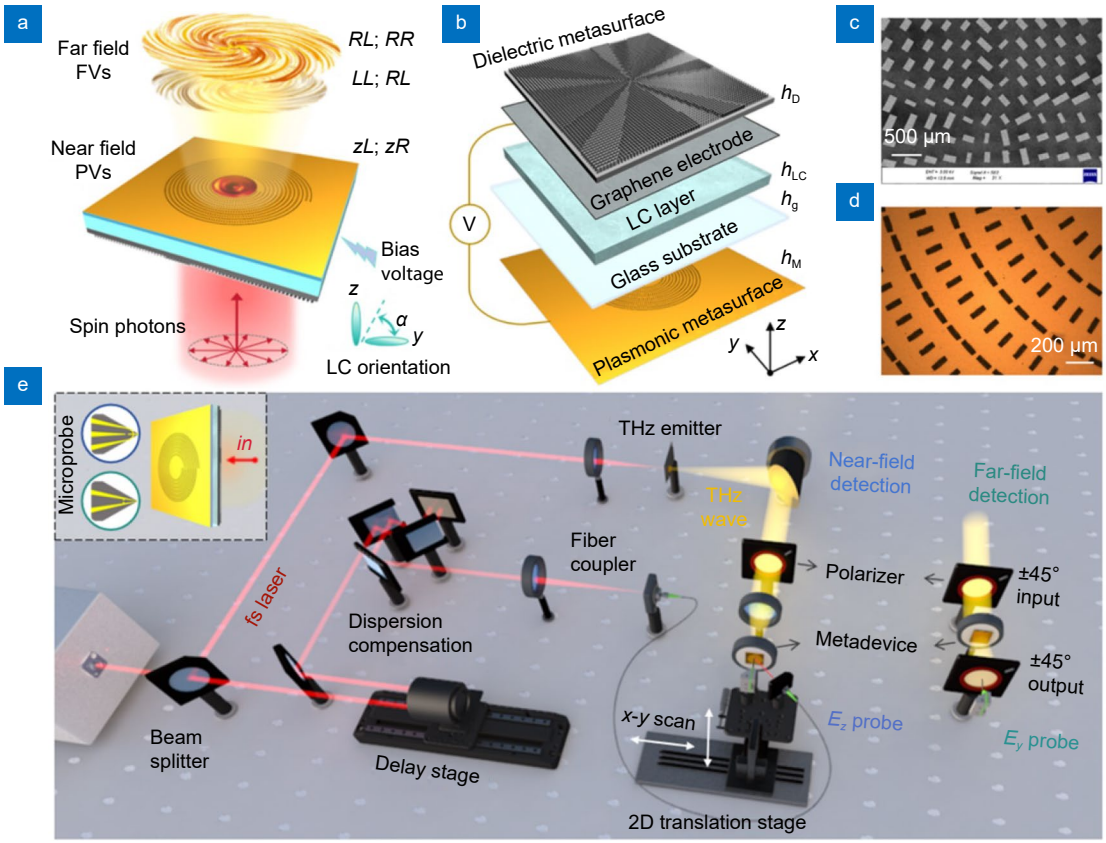

Fig. 1 | Schematic diagram of the proposed metadevice and the experimental setup. (**a**) The functional diagram of the LC-integrated cascaded metadevice with 6 spin-dependent vortex channels. (**b**) The detailed structure of the metadevice; Micrographs of (**c**) dielectric metasurface and (**d**) plasmonic metasurface. (**e**) Schematic diagram of N/F-STS system, in which the measurement methods of NF and FF are illustrated.

all-dielectric metasurface (Fig. 1(c)), composed of pillars etched on a high resistance Si substrate with a total thickness of h_D; 2) The graphene conductive layer at the bottom of the Si substrate, which acts as one of the electrodes with a high THz transmittance and a certain conductivity; 3) LC layer, designed to serve as a THz half-wave plate (HWP), and two PI orientation layers are on the upper and lower surfaces of LC layer to arrange LC molecules along the y direction when no external electric field is applied; 4) the plasmonic metasurface on a glass substrate (Fig. 1(d)), which is fabricated by ultraviolet laser etching on a copper film with a thickness of h_M. The metallic film of this metasurface acts as the other electrode. When a bias is applied between the electrodes, the LC rotates from the y-axis to the z-axis. As shown in Fig. 1(e), to measure the PVs and FVs, respectively, the GaAs photoconductive antenna probes for E_z and E_y detection are used in the near/far-field scanning THz spectroscopy (N/F-STS) system. The detailed device fabrication and experimental systems are described in the Section *Methods*.

The basic element of the plasmonic metasurface is subwavelength slits in the metallic film, which has a dipolar resonance response with its polarization direction always perpendicular to the slit orientation as shown in Fig. 2(a). This NF resonance excites an SPW that propagates along the metal surface, and a linearly polarized (LP) light radiates to the FF as an extraordinary optical transmission effect at the central frequency f_0 = 0.475 THz, where the peak transmittance reaches 90% and 70% in the simulation and experiment, respectively. Thus, the plasmonic metasurface can achieve both NF and FF wavefront control around 0.475 THz. Its schematic diagram is displayed in Fig. 2(b), which consists of 6-ring spiral-arrayed slit pair resonators (k = 1–6 from the inside to the outside). The m^{th} pair of slits in the k^{th} ring are arranged with perpendicular orientations ($\theta_{1,m}$ and $\theta_{2,m}$) and spaced at a distance d of half the SP wavelength, making sure the phase of the excited SPWs can be assigned in the whole 2π range under a circular polarized (CP) incidence. The detailed design can be found in Section 1 of Supplementary information.

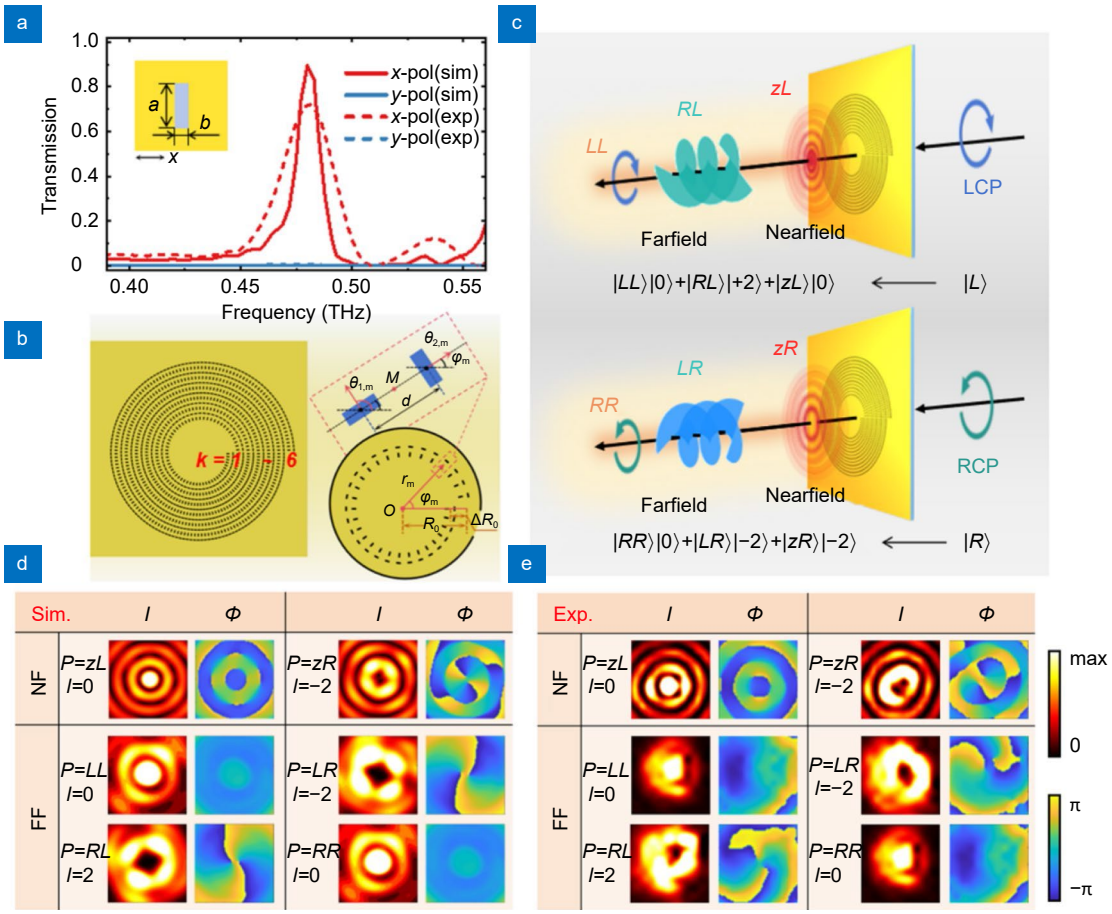

Fig. 2 | Structure scheme of the single plasmonic metasurface layer and its performances. (**a**) Simulated and experimental anisotropic transmission spectrum of metal slit array with a=160 μm, b=50 μm. (**b**) Schematic diagram of the plasmonic metasurface, the right part is the detailed diagrams of paired slits and the k^{th} spiral-arrayed slit pair resonator. (**c**) The function of a single plasmonic metasurface layer. (**d**) Simulated and (**e**) experimental NF/FF intensity and phase distributions at f_0=0.475 THz.

For the NF, the orientation of slit pairs introduces spin-dependent geometric phases. Besides, the on-chip distance difference from slit pairs to the center produces the propagation phase gradient of SPWs. Thus spin-decoupled PVs are obtained by arranging the positions and setting the rotation angles of m slit pairs, which are determined by the radius r_m and azimuth angle φ_m. In our design, each ring contributes to the geometric phase shift across a whole turn of $2\pi\sigma$ rad and the propagation phase of -2π rad along the azimuthal direction. As schematically shown in Fig. 2(c), this plasmonic metasurface generates PVs with orders satisfied as Eq. (1) (The detailed theoretical derivation can be found in Section 1 of Supplementary information):

$$l_{\mathrm{M,NF}} = \sigma - 1\,, \tag{1}$$

where the subscript M represents the plasmonic metasurface, l and σ represent quantum numbers of OAM and SAM, respectively. That is, l is the topological charge number, and $\sigma = \{+1, -1\}$ corresponds to the left- and right-handed spin states. Therefore, the 2 NF channels of PVs are yielded with $l_{\mathrm{M,NF}} = 0$ and -2 by plugging in $\sigma = \pm 1$. As shown in Fig. 2(d) and 2(e), the simulated and experimental results show that the PVs of (P=zL, l=0) and (P=zR, l=−2) are excited when incident photons are the L and R spin states (i.e. $\sigma = \pm 1$), respectively. The detailed methods of the simulation and measurements can be found in Section *Methods*. Importantly, the propagation phase of the progressive helical structures of the plasmonic metasurface leads to the on-chip spin-decoupling, and provides parity breaking of the 2 PV OAMs (i.e. the values of l do not occur in ± pairs to the incident spin states $\sigma = \pm 1$).

Meanwhile, this propagation phase on the helical plasmonic metasurface is negligible in the FF. As the derivation shown in Section 1 of Supplementary information, the total FF transmitting process can be expressed as

follows:

$$\begin{bmatrix} E_{\mathrm{M,Lout}} \\ E_{\mathrm{M,Rout}} \end{bmatrix} = \begin{bmatrix} t_{\mathrm{co}} & t_{\mathrm{cro}}\mathrm{e}^{-\mathrm{i}2\varphi_{\mathrm{M}}} \\ t_{\mathrm{cro}}\mathrm{e}^{\mathrm{i}2\varphi_{\mathrm{M}}} & t_{\mathrm{co}} \end{bmatrix} \begin{bmatrix} E_{\mathrm{M,Lin}} \\ E_{\mathrm{M,Rin}} \end{bmatrix}, \quad (2)$$

where t_{co} and t_{cro} are transmission coefficients of spin-locked components (E_{LL} and E_{RR}) and the spin-flipped components (E_{RL} and E_{LR}), respectively. It's worth mentioning that the spin-flipped components stem from the resonance response of structured metal slits, inducing a geometric phase of $4\pi\sigma$ by spin-orbital angular momentum coupling across a whole turn. The spin-locked components pass through the slits as the Gaussian beam, with no phase shift. Thus, they are called the direct-transmission terms. Four FF channels of FVs are formed according to different spin states, of which topological charges can be described as Eq. (3):

$$l_{\mathrm{M,FF}} = \begin{cases} 2\sigma, (\mathrm{resonance\ terms}) \\ 0, (\mathrm{direct-transmission\ terms}) \end{cases}. \quad (3)$$

Since the asymmetry in the progressive helical structure has been ignored in the FF (the propagation phase is no longer introduced), the FVs are spin-coupled and the $l_{\mathrm{M,FF}}$ is in parity conservation. As shown in Fig. 2(d) and 2(e), the FF performs FV modes of (P=RL, l=2), (P=LL, l=0), (P=LR, l=−2) and (P=RR, l=0). It is seen that the energy distribution of four FV terms is of the same magnitude order. Both PVs and FVs can be generated efficiently with high purity, and the transmission efficiency of the metasurface is further discussed in Section 3 of Supplementary information.

Single dielectric metasurface

Furthermore, as depicted in Fig. 3(a), the single dielectric metasurface is discussed, which introduces an inversion asymmetrical phase distribution in front of the plasmonic metasurface. The meta-atom is constructed by a rectangular pillar on the substrate with period p. Its spatial phase includes the dynamic phase and the geometric phase, which stems from the geometric dimensions $w \times q$ and orientation angle β, respectively. According to Eq. (4), $\beta = (u-v)\varphi_{\mathrm{D}}/4$, $\Phi_x = (u+v)\varphi_{\mathrm{D}}/2$, and $\Delta\Phi_{xy} = \pi$, then a series of pillars with the HWP function can be selected and arranged:

$$\begin{aligned} \begin{bmatrix} E_{\mathrm{D,Lout}} \\ E_{\mathrm{D,Rout}} \end{bmatrix} &= \begin{bmatrix} 0 & \mathrm{e}^{\mathrm{i}v\varphi_{\mathrm{D}}} \\ \mathrm{e}^{\mathrm{i}u\varphi_{\mathrm{D}}} & 0 \end{bmatrix} \begin{bmatrix} E_{\mathrm{D,Lin}} \\ E_{\mathrm{D,Rin}} \end{bmatrix} \\ &= \begin{bmatrix} 0 & \mathrm{e}^{\mathrm{i}(\Phi_x - 2\beta)} \\ \mathrm{e}^{\mathrm{i}(\Phi_x + 2\beta)} & 0 \end{bmatrix} \begin{bmatrix} E_{\mathrm{D,Lin}} \\ E_{\mathrm{D,Rin}} \end{bmatrix}, \end{aligned} \quad (4)$$

where the subscript D represents the dielectric metasurface, φ_{D} represents the azimuthal angle of the dielectric layer, Φ_x and Φ_y is the phase shift in the x- and y- direction. In this case, the dielectric metasurface generates FVs with orders as follows, which achieves spin-decoupling of the output FV modes.

$$l_{\mathrm{D,FF}} = \begin{cases} u, (\sigma = 1) \\ v, (\sigma = -1) \end{cases}. \quad (5)$$

The characterizations in simulation at f_0 = 0.475 THz are shown in Fig. 3(b–d). The final selection of geometric sizes can be found in Section 2 of Supplementary information. In this work, the dielectric metasurface is

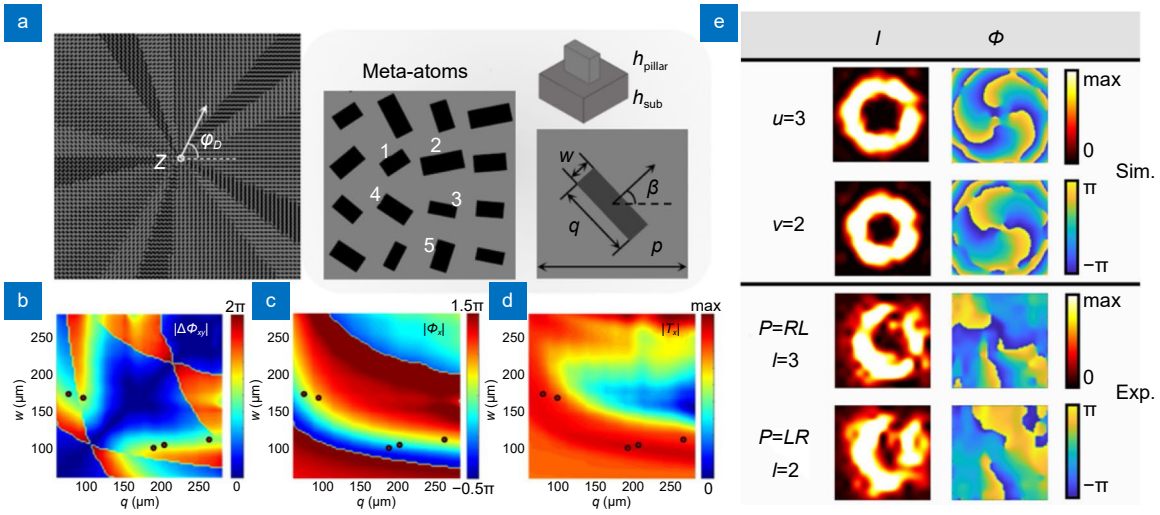

Fig. 3 | Structure scheme of the single dielectric metasurface and its performance results. (**a**) Schematic diagram of spin-decoupled all-dielectric metasurface containing pillars with 5 geometric sizes. Inset: perspective and top views of meta-atoms. (**b**) The simulated anisotropic phase delays, (**c**) phase shifts, and (**d**) transmission coefficients in the x direction under 45°-LP incidence when the width w and the length q are swept from 60 μm to 280 μm. The selected rectangle pillars are marked with dots. (**e**) The simulated and experimental FF intensity and phase distribution.

designed with the parameters of u = 3 and v = 2, which has a high transmission efficiency for FV generation shown in Section 3 of Supplementary information. Most of the transmission energy is concentrated in the spin-flipped components, while the spin-locked energy is very weak. As presented in Fig. 3(e), its simulated results of intensity and phase distributions are in agreement with the experimental ones, obtaining modes with (P=RL, l=3) and (P=LR, l=2). The differences between simulation and experiment mainly originate from the fabrication error of dielectric metasurface.

Cascaded metadevice

Next, the cascaded metadevice is investigated in its entirety. The LC integration provides an effective strategy for dynamic spin transformation, and its thickness h_{LC} is designed to enable the anisotropic phase difference of π rad at the center frequency f_0. As shown in Fig. 1(a), the angle between the main axis of LC molecules and the y-axis in the y-z plane is defined as α. The vortex mode can be described as $|P_{\mathrm{out}}P_{\mathrm{in}}\rangle\,|l\rangle$. $|P_{\mathrm{out}}P_{\mathrm{in}}\rangle$ stands for the input and output photon states, which can be replaced by $|zs\rangle$ for PVs, $|ss\rangle$ and $|s^*s\rangle$ for FVs. Wherein, s represents the spin states incident to the metadevice, that is, L or R (L^*=R), corresponding to σ = +1 or σ = −1. The photon with an incident spin state $|s\rangle$ exits the dielectric metasurface, carrying the FV mode $|s^*s\rangle\,|l_{\mathrm{D}}\rangle$. When E_z = 0 V/mm or 35 V/mm, the corresponding value is α = 0° or 90°, and the LC layer flips the spin state or not, respectively. In the corresponding condition, a photonic state of $|s\rangle$ or $|s^*\rangle$ will be incident to the plasmonic metasurface, and the corresponding PV mode is $|zs\rangle\,|\sigma-1\rangle$ or $|zs\rangle\,|-\sigma-1\rangle$ based on Eq. (1). The FV modes including the resonance terms and direct-transmission terms are $|s^*s\rangle\,|2\sigma\rangle$ and $|ss\rangle\,|0\rangle$ for the former case, while those are $|ss\rangle\,|-2\sigma\rangle$ and $|s^*s\rangle\,|0\rangle$ for the latter case based on Eq. (3). Therefore, considering the total vortex field of the whole metadevice, based on spin-orbital angular momentum coupling and photon state superposition, the mapping in both NF and FF can be described as:

$$|s\rangle \rightarrow \begin{cases} |zs\rangle\,|l_{\mathrm{D}}+\sigma-1\rangle + |s^*s\rangle\,|l_{\mathrm{D}}+2\sigma\rangle + |ss\rangle\,|l_{\mathrm{D}}\rangle \\ \text{when } \alpha = 0^\circ, \\ |zs\rangle\,|l_{\mathrm{D}}-\sigma-1\rangle + |s^*s\rangle\,|l_{\mathrm{D}}\rangle + |ss\rangle\,|l_{\mathrm{D}}-2\sigma\rangle \\ \text{when } \alpha = 90^\circ. \end{cases} \tag{6}$$

To simplify the expression in the following text, the channels are described by the photon states. Therefore, 6 independent vortex channels are constructed associated with spin states and the NF/FF field spatial positions, including NF channels of {zL; zR}, and FF channels of {LL; RL; LR; RR}. Additionally, it can be found that the OAMs with parity symmetry breaking can be realized both in NF and in FF. But differently, for the NF, it is caused by the inversion symmetry breaking of the plasmonic metasurface structure, while for the FF, it results from that of the dielectric metasurface. Finally, the output vortices with completely different orders are brought by the superposition of photon states.

Considering that the LC causes the input spin states to switch between the two extreme states, this device can obtain 12 different vortex modes in these 6 channels in theory. For incident L and R spin states, two sets of the parameters $s = L, \sigma = +1, l_{\mathrm{D,L}} = 3$ and $s = R, \sigma = -1, l_{\mathrm{D,R}} = 2$ are substituted into Eq. (6). For LC along the y-axis (α = 0°), since the LC flips the spin state but does not change the vortex order, vortex modes in 6 channels are as follows: $|zL\rangle\,|3\rangle$, $|RL\rangle\,|5\rangle$, $|LL\rangle\,|3\rangle$, $|zR\rangle\,|0\rangle$, $|LR\rangle\,|0\rangle$, $|RR\rangle\,|2\rangle$. For the other case that LC is oriented along the z-axis (α=90°), the vortex modes in 6 channels are $|zL\rangle\,|1\rangle$, $|RL\rangle\,|3\rangle$, $|LL\rangle\,|1\rangle$, $|zR\rangle\,|2\rangle$, $|LR\rangle\,|2\rangle$, $|RR\rangle\,|4\rangle$. These 12 vortices obtained in simulations and experiments are illustrated in Fig. 4(a) and 4(b). The intensity distribution exhibits an obvious hollow ring, of which the diameter is related to the topological charge number. Besides, the phase distribution of the l-ordered vortex is $2\pi l$ across a whole turn of the center. The field intensity and phase distribution corresponding to each spin state in Fig. 4(a) and 4(b) are consistent with the vortex modes analyzed theoretically. In simulations and experiments, the values of these topological charge numbers are positive, indicating that the parity symmetry is broken. This device works in an operating bandwidth of 0.44–0.52 THz, and the results at other frequencies are shown in Section 5 of Supplementary information. In addition, due to the spatial separation of NF and FF as well as the differences in vortex orders, it is conducive to the demultiplexing of coaxial channels, which means that an extra mode filter is not required, and the extraction of OAM could be realized by spin decoupling and polarization detection.

Furthermore, to evaluate the performance of the proposed device, we focus on the mode purity and the crosstalk of vortices in the independent channels. The total NF and FF can be regarded as the superposition of

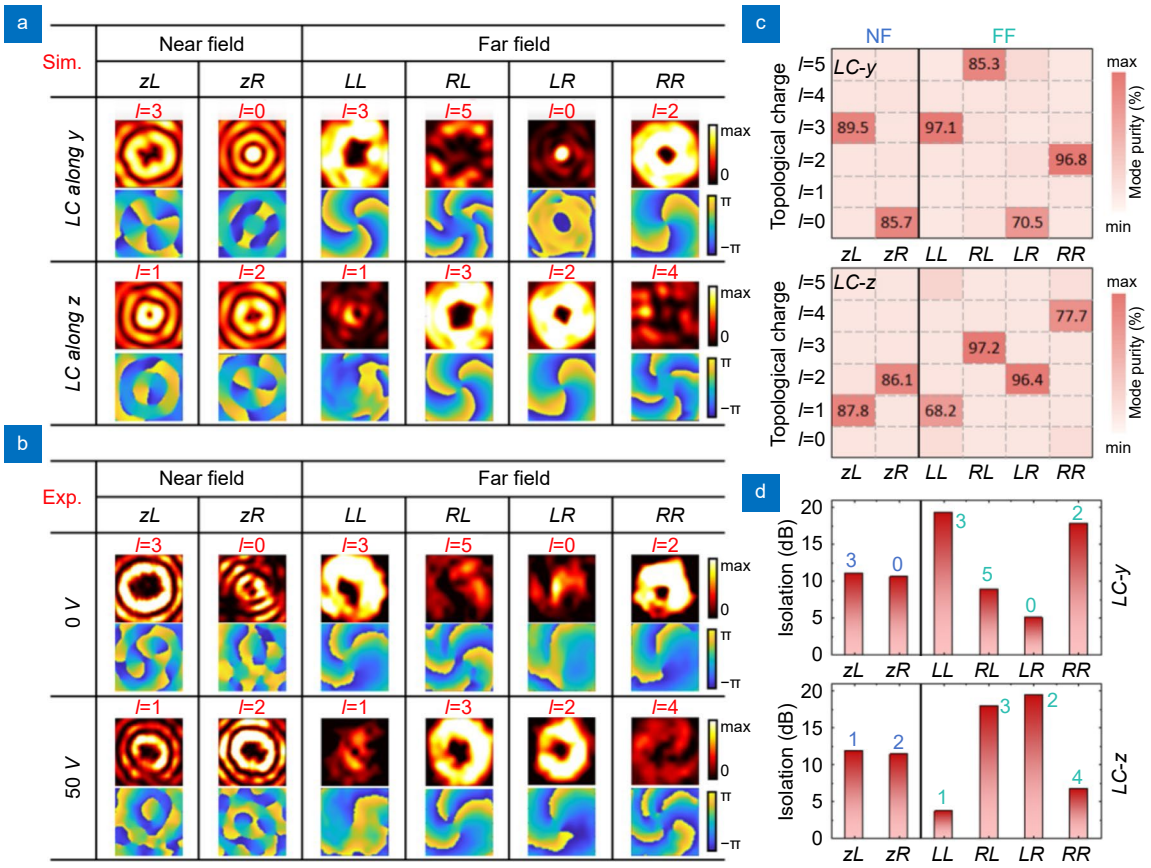

Fig. 4 | Results and evaluations of designed cascaded metadevice. (**a**) The simulated and (**b**) experimental intensity and phase distribution of 12-mode vortices at the central frequency f_0. (**c**) The vortex mode purity matrix and (**d**) isolation of 6 channels in simulation when the LC orientation is along the *y*- and *z*-axis.

various vortex modes, whose amplitudes approximately follow the *l*-th order Bessel function for a specified photon state: $E_{z,\mathrm{NF}}(\rho,\phi)=\sum c_{l_\mathrm{N}}\mathrm{J}_{l_\mathrm{N}}(k_\mathrm{SP}\rho)\mathrm{e}^{\mathrm{i}l_\mathrm{N}\phi}$, $E_{\mathrm{FF}}(\rho,\phi)=\sum c_{l_\mathrm{F}}\mathrm{J}_{l_\mathrm{F}}(k_0\rho)\mathrm{e}^{\mathrm{i}l_\mathrm{F}\phi}$, where $(\rho,\ \phi)$ is the polar coordinates in the *x*-*y* plane, k_sp and k_0 are wavevectors of SPWs and free-space waves, c_{l_N} and c_{l_F} are proportionality factors of the l_N-th PVs and l_F-th FVs. The mode purity is defined as:

$$\eta(\%)=I_\mathrm{t}\Big/\sum\nolimits_\mathrm{S}I_\mathrm{l}\ , \tag{7}$$

in which I_t is the intensity of the targeted vortex, calculated by $I_\mathrm{l}=2\pi\int|c_\mathrm{l}\mathrm{J}_\mathrm{l}(k\rho)|^2\rho\mathrm{d}\rho$, and $\sum_\mathrm{S}I_\mathrm{l}$ is the total intensity within the finite aperture. The isolation of each channel is calculated by $Iso(\mathrm{dB})=10\log(I_\mathrm{t}/\sum I_\mathrm{cros})$, $\sum I_\mathrm{cros}$ is the sum of the intensities of all crosstalk aroused by other non-target vortices.

Based on these evaluation indexes, we quantitatively analyze the quality of 12-mode vortices. The generation intensity matrix of the 6 multiplexed channels is shown in Fig. 4(c), when LC is oriented along the *y*- and *z*-axis. The highlight of the matrix is the mode purity of the correct-ordered vortex, and the others are crosstalk. The results show that the average mode purity of PVs and FVs is above 85%. Moreover, the maximum isolation degree is 11.9 dB and 19.5 dB in the NF/FF channels, as shown in Fig. 4(d). Notably, the isolations of two direct-transmission FV terms are very high, but the other resonance terms are with lower isolation. The reason is that the spin-orbital angular momentum coupling, makes PVs and the resonance terms of FVs subject to the coupling efficiency from incident free-space waves to SPWs, while the direct transmission terms of FVs are spin-independent and fully transmit the input modes. Generally, the proposed device achieves high-purity excitation of the expected vortices with great isolations.

Active modulation

In this section, the dynamic modulation capabilities are investigated in 6 channels of spin multiplexing and NF/FF multiplexing. Fig. 5(a) shows the PVs modulation

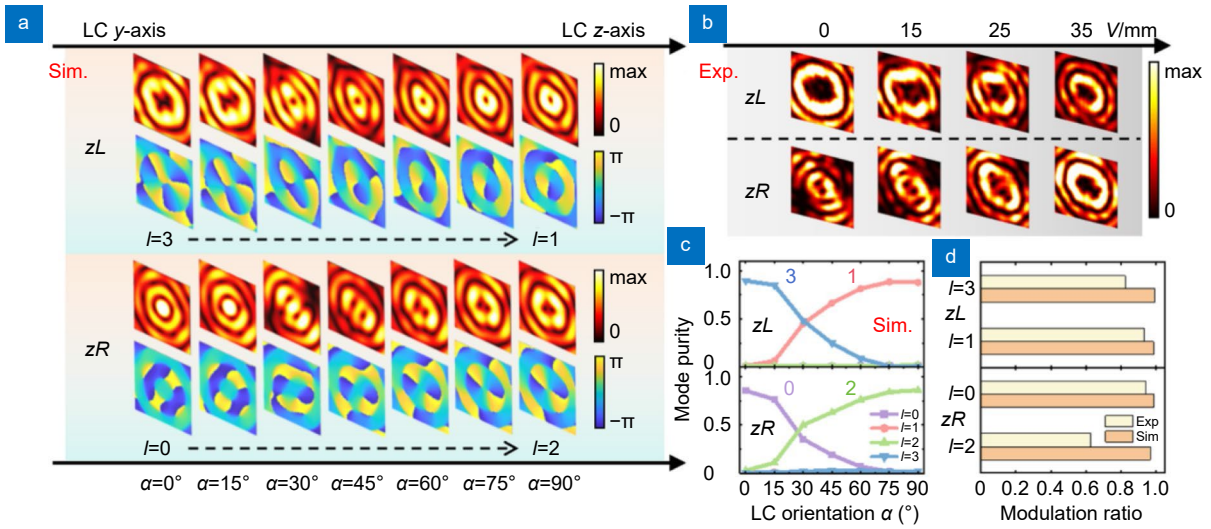

Fig. 5 | Illustrations of the active modulation in the 2 NF channels. With the LC orientation rotating in the *y*-*z* plane, (**a**) the simulated evolution process of the intensity and phase distributions of PVs with $P = zL$ and zR at the frequency f_0. (**b**) the measured evolution process of intensity distributions. (**c**) The dynamic modulation process of the mode purity for PVs in simulation. (**d**) Simulated and experimental modulation ratio of the expected PV modes.

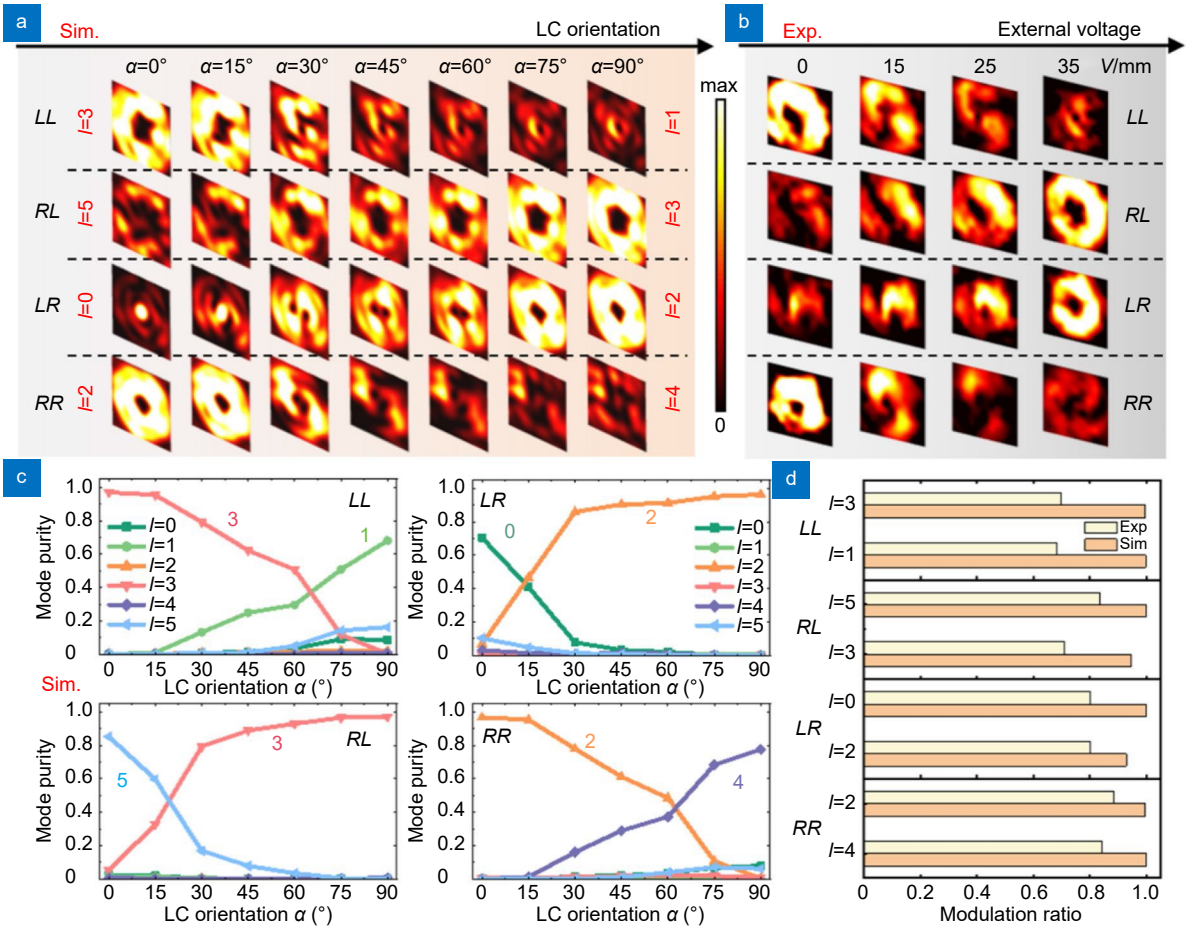

Fig. 6 | Illustrations of the active modulation in the 4 FF channels. With the LC orientation rotating in the *y*-*z* plane, the (**a**) simulated and (**b**) measured evolution process of the intensity distributions at the frequency f_0. (**c**) The dynamic modulation process of the mode purity for FVs in simulation. (**d**) Simulated and experimental modulation ratio of the expected FV modes.

process in 2 NF channels in simulations. LC orientation is set to α = 0°–90° to simulate the process of applying the external electric voltage in experiments. Vortices in each channel are with the modes of a fixed spin state but tunable orders. It is seen that the diameter of the intensity ring and the phase distribution evolve gradually. In the *zL* channel, the order of PVs changes from 3 to 1 with the reduction of the ring shape. In another *zR* channel, the order changes from 0 to 2. Fig. 5(b) shows the measured NF distribution evolution, as the bias electric voltage increases from 0 V/mm to 35 V/mm, which is consistent with the simulation results. For the FF channels of {*LL; RL; LR; RR*}, Fig. 6(a) and 6(b) demonstrated the evolution of the simulated and experimental intensity distribution, which shows the topological charge of FVs gradually changes from {3; 5; 0; 2} to {1; 3; 2; 4}. The corresponding phase modulation diagrams are presented in Section 5 of Supplementary information.

Actually, for the intermediate state during the modulation process, the field distribution is an interfered field between the 2 vortices with different weights. Fig. 5(c) and 6(c) show the simulated dynamic change process of mode purity in each channel of NF and FF, respectively. It is indicated that the energy is mainly transferred between the expected two modes. The experimental mode purity results of the modulated vortices can be found in Fig. S3 of Supplementary information. Additionally, the achieved vortex order before and after the conversion is asymmetric. Especially, it can be found that the gradient of transformation is with conjugate antisymmetric, that is, $\Delta l_{zL} = -\Delta l_{zR} = 2$, $\Delta l_{LL} = \Delta l_{RR} = -\Delta l_{LR} = -\Delta l_{RL} = -2$. Essentially, it is related to the spin-dependent geometric phase distribution on the chip and in the free space, which is mirror symmetric both in NF and FF. Therefore, the device can realize the active proportional distribution of the energy between two modes in any channel.

Furthermore, the modulation ratio is another important index defined as

$$MR(\%) = (\eta_{\max} - \eta_{\min}) / \eta_{\max} , \tag{8}$$

to describe the change rate of the purity of a vortex mode during the active tuning process, where $\eta_{\max}$ and $\eta_{\min}$ are the maximum and minimum mode purity. As illustrated in Fig. 5(d) and 6(d), the simulated modulation ratios of 12 mode vortices achieve over 90%. And the measured modulation ratio on average reaches 70% in the 6 channels. In addition, the maximum ratio of PVs is 94.1% for the mode $|zR\rangle\,|0\rangle$. And that of FVs is 88.4% for the mode $|RR\rangle\,|2\rangle$. As a result, this metadevice exhibits the dynamic switching and energy distribution of 4-mode PVs and 8-mode FVs.

Conclusions

In conclusion, a cascaded dielectric-LC-plasmonic metadevice is proposed to construct multiple independent vortex channels associated with the spin states and the NF/FF positions. The mechanism and function of this device are as follows: 1) The cascaded metadevice achieves PV and FV generations by spin-orbital angular momentum coupling and photonic state superposition. 2) The asymmetric helical structures of the plasmonic and dielectric metasurfaces bring about the broken parity conservation of PV modes and FV modes, respectively. 3) 12 vortex modes obtained in 6 channels and the active mode switch are realized by the LC tunable orientation. The theoretical calculation, numerical simulation, and experimental characterization of the N/F-STS system have firmly verified that PVs and FVs are generated with high mode purity of over 85% on average with a maximum isolation of 11.9 dB and 19.5 dB for NF and FF, respectively, and the measured modulation ratios are above 70%. This work provides an efficient and compact platform for integrated THz multi-channel on-chip device, and paves the way for multi-parameter multiplexing and active manipulation in high-capacity THz communication systems.

Methods

Numerical simulation: Numerical simulations are performed by utilizing the finite-difference time-domain (FDTD) method in the commercial software Lumerical FDTD Solution. Boundaries at *x, y,* and *z* directions are surrounded by perfectly matched layers. The refractive index of Si and glass is set to 3.42 and 1.9, and the copper can be viewed as a perfect electrical conductor (PEC). The LC layer is modeled as a medium with uniaxial anisotropy, of which the extraordinary and ordinary refractive indices (n_e and n_o) are set to 1.9 and 1.6, respectively. In this work, the main axis of LC is set to rotate from the *y*- to *z*-axis. Surface monitors set in the *x*-*y* plane are placed 50 μm and 4 cm, respectively, to directly obtain the intensity and phase distributions of longitudinal (*z*-) near field and transversal (*x*-, *y*-) far field. It is worth to be mentioned that, the spin components can be synthesized by the [E_x, E_y] as orthogonal bases.

Device fabrication: The all-dielectric metasurface is fabricated by the ultraviolet lithography process and reactive ion beam etching on a high-resistance Si wafer with its thickness h_D = 1 mm. The meta-atoms have a period of p =300 μm and a height of h_{pillar} =500 μm. The plasmonic metasurface is fabricated by laser direct writing process, of which the structured metallic film with ion sputtering thickness of h_M = 100 nm. The glass substrate with h_g= 500 μm used in this work is JGS1-type fused silica glass, which has an excellent transmission characteristic in the THz band. LC is filled in the cell between the substrates of these two metasurfaces encapsulated by the ultraviolet glue. The LC used in this work is a high birefringence LC (HTD028200) from Jiangsu Hecheng Technology Co., Ltd., and its birefringence is Δn= 0.3. The thickness h_{LC} is designed as 1050 μm to get an anisotropic phase difference of π rad at the central frequency f_0 = 0.475 THz. To induce out-of-plane orientation of the LC molecules rotating in the *y*-*z* plane, the graphene solution (G139799), from Shanghai Aladdin Biochemical Technology Co., Ltd. is spin-coated on the Si substrate, which forms a porous graphene conductive layer after heating and drying. It alternately serves as the positive and negative electrodes, cooperating with the metallic film. A square wave voltage is applied with a frequency of 500 Hz and the maximum electric field is 35 V/mm to drive liquid crystal molecules to rotate from the *y* to *z*-axis. These layers of two metasurfaces and the LC layer are all tightly cascaded with no spacing, and the total size of the device is 20 mm × 20 mm × 2.35 mm.

Experimental setup: We carry out the experiments in the N/F-STS system. The excitation source is a femtosecond laser with 780 nm wavelength and 80 fs duration. Two types of photoconductive probes, the longitudinal and transversal field microprobe (TeraSpike TD-800-*X* and TD-800-*Z*, from Protemics Company, Aachen, Germany) are capable of detecting SPWs and free space beams, respectively. They are fixed on the two-dimensional translation platform to allow mapping of the NF/FF distribution. The tips of probes are metal cone slits along the *z*- and *y*-axis, respectively, as illustrated in the left dotted box. In this work, the probes were located 50 μm and 4 cm away from the metadevice to detect the E_z component for NF and E_y component for FF, respectively. The mapping range is 2 mm×2 mm for NF with the scanning step of 0.15 mm, and 14 mm×14 mm for FF with the scanning step of 1 mm. The mapping pixels are calculated after the interpolation algorithm with a ratio of 1∶10. To obtain the complete spin-state responses of the metadevice, the two THz metal wire polarizers are added before and after the metadevice to get the ±45° LP component of FVs. The time domain signal was obtained point by point in space, and then the amplitude and phase information of the whole image at a frequency was obtained after the Fourier transform. The data processing method is provided in Section 4 of Supplementary information.

Abbreviations: The definitions and the abbreviations of the key concepts are specificated in Section 6 of Supplementary information.

References

1. Guerboukha H, Cao Y, Nallappan K et al. Super-resolution orthogonal deterministic imaging technique for terahertz subwavelength microscopy. *ACS Photonics* **7**, 1866–1875 (2020).
2. Nagatsuma T, Ducournau G, Renaud CC. Advances in terahertz communications accelerated by photonics. *Nat Photonics* **10**, 371–379 (2016).
3. Zhang YQ, Min CJ, Dou XJ et al. Plasmonic tweezers: for nanoscale optical trapping and beyond. *Light Sci Appl* **10**, 59 (2021).
4. Deng WT, Chen L, Zhang HQ et al. On-chip polarization- and frequency-division demultiplexing for multidimensional terahertz communication. *Laser Photonics Rev* **16**, 2200136 (2022).
5. Yao AM, Padgett MJ. Orbital angular momentum: origins, behavior and applications. *Adv Opt Photonics* **3**, 161–204 (2011).
6. Zhang X, Huang LL, Zhao RZ et al. Basis function approach for diffractive pattern generation with Dammann vortex metasurfaces. *Sci Adv* **8**, eabp8073 (2022).
7. Zhang YQ, Zeng XY, Ma L et al. Manipulation for superposition of orbital angular momentum states in surface plasmon polaritons. *Adv Opt Mater* **7**, 1900372 (2019).
8. Zang XF, Zhu YM, Mao CX et al. Manipulating terahertz plasmonic vortex based on geometric and dynamic phase. *Adv Opt Mater* **7**, 1801328 (2019).
9. Mei F, Qu GY, Sha XB et al. Cascaded metasurfaces for high-purity vortex generation. *Nat Commun* **14**, 6410 (2023).
10. Zhao RZ, Xiao XF, Geng GZ et al. Polarization and holography recording in real-and *k*-space based on dielectric metasurface. *Adv Funct Mater* **31**, 2100406 (2021).
11. Cai XD, Tang R, Zhou HY et al. Dynamically controlling terahertz wavefronts with cascaded metasurfaces. *Adv Photonics* **3**, 036003 (2021).
12. Han J, Xu YH, Zhang HF et al. Tailorable polarization-dependent directional coupling of surface plasmons. *Adv Funct Mater* **32**, 2111000 (2022).
13. Zhang XQ, Xu Q, Xia LB et al. Terahertz surface plasmonic waves: a review. *Adv Photonics* **2**, 014001 (2020).
14. Wu T, Xu Q, Zhang XQ et al. Spin-decoupled interference metasurfaces for complete complex-vectorial-field control and five-channel imaging. *Adv Sci* **9**, 2204664 (2022).
15. Li GX, Kang M, Chen SM et al. Spin-enabled plasmonic metasurfaces for manipulating orbital angular momentum of light. *Nano Lett* **13**, 4148–4151 (2013).
16. Li XY, Chen C, Guo YH et al. Monolithic spiral metalens for ultrahigh-capacity and single-shot sorting of full angular momen-

tum state. *Adv Funct Mater* **34**, 2311286 (2024).
17. Lang YH, Xu Q, Chen XY et al. On-chip plasmonic vortex interferometers. *Laser Photonics Rev* **16**, 2200242 (2022).
18. Jiang XH, Xu Q, Lang YH et al. Geometric phase control of surface plasmons by dipole sources. *Laser Photonics Rev* **17**, 2200948 (2023).
19. Spektor G, Kilbane D, Mahro AK et al. Revealing the subfemtosecond dynamics of orbital angular momentum in nanoplasmonic vortices. *Science* **355**, 1187–1191 (2017).
20. Kim H, Park J, Cho SW et al. Synthesis and dynamic switching of surface Plasmon vortices with plasmonic vortex lens. *Nano Lett* **10**, 529–536 (2010).
21. Guo YH, Zhang SC, Pu MB et al. Spin-decoupled metasurface for simultaneous detection of spin and orbital angular momenta via momentum transformation. *Light Sci Appl* **10**, 63 (2021).
22. Devlin RC, Ambrosio A, Rubin NA et al. Arbitrary spin-to–orbital angular momentum conversion of light. *Science* **358**, 896–901 (2017).
23. Zhang H, Sha XB, Chen QM et al. All-dielectric metasurface-enabled multiple vortex emissions. *Adv Mater* **34**, 2109255 (2022).
24. Prinz E, Spektor G, Hartelt M et al. Functional meta lenses for compound plasmonic vortex field generation and control. *Nano Lett* **21**, 3941–3946 (2021).
25. Yuan XY, Xu Q, Lang YH et al. Temporally deuterogenic plasmonic vortices. *Nanophotonics* **13**, 955–963 (2024).
26. Yuan XY, Xu Q, Lang YH et al. Tailoring spatiotemporal dynamics of plasmonic vortices. *Opto-Electron Adv* **6**, 220133 (2023).
27. Zhao H, Quan BG, Wang XK et al. Demonstration of orbital angular momentum multiplexing and demultiplexing based on a metasurface in the terahertz band. *ACS Photonics* **5**, 1726–1732 (2018).
28. Liu Y, Chen L, Zhou CX et al. Theoretical study on generation of multidimensional focused and vector vortex beams via all-dielectric spin-multiplexed metasurface. *Nanomaterials* **12**, 580 (2022).
29. Zhao H, Wang XK, Liu ST et al. Highly efficient vectorial field manipulation using a transmitted tri-layer metasurface in the terahertz band. *Opto-Electron Adv* **6**, 220012 (2023).
30. Liu WY, Jiang XH, Xu Q et al. All-dielectric terahertz metasurfaces for multi-dimensional multiplexing and demultiplexing. *Laser Photonics Rev* **18**, 2301061 (2024).
31. Jiang Q, Bao YJ, Li J et al. Bi-channel near- and far-field optical vortex generator based on a single plasmonic metasurface. *Photonics Res* **8**, 986–994 (2020).
32. Dai CH, Liu T, Wang DY et al. Multiplexing near- and far-field functionalities with high-efficiency bi-channel metasurfaces. *PhotoniX* **5**, 11 (2024).
33. Sun PZ, Liu BH, Wang YF et al. Ultrabroadband multichannel vector vortex beams with versatile electrically induced functionality. *Laser Photonics Rev* **17**, 2300098 (2023).
34. Li CQ, Song ZY. Tailoring terahertz wavefront with state switching in VO_2 Pancharatnam–Berry metasurfaces. *Opt Laser Technol* **157**, 108764 (2023).
35. Zhou ZK, Song ZY. Terahertz mode switching of spin reflection and vortex beams based on graphene metasurfaces. *Optics Laser Technol* **153**, 108278 (2022).
36. Zhuang XL, Zhang W, Wang KM et al. Active terahertz beam steering based on mechanical deformation of liquid crystal elastomer metasurface. *Light Sci Appl* **12**, 14 (2023).
37. Chen BW, Wang XR, Li WL et al. Electrically addressable integrated intelligent terahertz metasurface. *Sci Adv* **8**, eadd1296 (2022).
38. Guo JY, Wang T, Zhao H et al. Reconfigurable terahertz metasurface pure phase holograms. *Adv Opt Mater* **7**, 1801696 (2019).
39. Chen KX, Xu CT, Zhou Z et al. Multifunctional liquid crystal device for grayscale pattern display and holography with tunable spectral-response. *Laser Photonics Rev* **16**, 2100591 (2022).
40. Bosch M, Shcherbakov MR, Won K et al. Electrically actuated varifocal lens based on liquid-crystal-embedded dielectric metasurfaces. *Nano Lett* **21**, 3849–3856 (2021).
41. Shen ZX, Zhou SH, Li XN et al. Liquid crystal integrated metalens with tunable chromatic aberration. *Adv Photonics* **2**, 036002 (2020).
42. Wang S, Guo HB, Chen BW et al. Electrically active terahertz liquid-crystal metasurface for polarization vortex beam switching. *Laser Photonics Rev* **18**, 2301301 (2024).
43. Zhao HJ, Fan F, Wang YM et al. Vortex-vector beam conversion and chiral field manipulation based on terahertz liquid crystal cascaded metadevice. *Laser Photonics Rev* **18**, 2400442 (2024).
44. Wang YM, Fan F, Zhao HJ et al. Active broadband unidirectional focusing of terahertz surface plasmons based on a liquid-crystal-integrated on-chip metadevice. *Photonics Res* **12**, 2148–2157 (2024).

Acknowledgements

This work was supported by the National Natural Science Foundation of China (62335012, 62371258, 624B2075, 62205160, 62435010), Young Scientific and Technological Talents in Tianjin (QN20230227), Fundamental Research Funds for the Central Universities, Nankai University (63231159).

Author contributions

Y. M. Wang proposed the original idea and conducted the numerical calculations. F. Fan and Y. M. Wang designed the experiments and contributed to the theory and data analysis. Y. M. Wang and Y. Y. Ji performed the measurements. J. Liu and H. J. Zhao fabricated the samples. Y. M. Wang and F. Fan wrote the manuscript. F. Fan and S. J. Chang supervised the project. All authors discussed the results and commented on the manuscript.

Competing interests

The authors declare no competing financial interests.

Supplementary information

Supplementary information for this paper is available at https://doi.org/10.29026/oea.2025.240250

Scan for Article PDF